



Cite this: *Catal. Sci. Technol.*, 2026, **16**, 280

## Ring opening hydrogenolysis of 5-hydroxymethyl furfural over supported bimetallic catalysts

Heba Alsharif,<sup>ab</sup> Matthew Conway, Marina Chernova,<sup>c</sup> David J. Morgan, Javier Ruiz Martínez, Stuart H. Taylor and Meenakshisundaram Sankar \*<sup>a</sup>

The selective conversion of biomass-derived 5-hydroxymethylfurfural (HMF) to 1,6-hexanediol (1,6-HDO) is a promising pathway for sustainable production of chemicals from renewable feedstock. Here, we report the catalytic performance of various supported platinum catalysts, including monometallic Pt nanoparticles on different supports (CeO<sub>2</sub>, MgO, hydrotalcite, and hydroxyapatite) and bimetallic (PtPd, PtCo, PtRu, and PtRe) nanoparticles supported on hydroxyapatite for this reaction under batch reaction conditions. Among the monometallic catalysts, Pt supported on hydroxyapatite (Pt/HAP) demonstrated the highest selectivity (30%) for 1,6-HDO at 85% HMF conversion. This superior performance is attributed to the amphoteric properties of the hydroxyapatite support. Notably, the incorporation of Ru as a second metal in the Pt nanoparticles significantly improved catalytic efficiency. The bimetallic PtRu/HAP catalyst achieved an impressive selectivity of 62% for 1,6-HDO at 85% conversion. Characterization by X-ray Photoelectron Spectroscopy (XPS) and Electron Microscopy revealed that the addition of Ru to Pt nanoparticles resulted in smaller bimetallic nanoparticle sizes compared to monometallic Pt nanoparticles, contributing to the enhanced 1,6-HDO selectivity observed for the bimetallic system. The effects of reaction temperature and pressure on 1,6-hexanediol selectivity were also studied. Additionally, the acidity and basicity of the hydroxyapatite supported catalyst were analysed using the surface Ca/P ratio as well the CO<sub>2</sub> and NH<sub>3</sub> TPD data. The results show that the PtRu/HAP catalyst has optimal acidic site density and least basic sites compared to the monometallic catalysts. This unique combination of acidic and basic surface properties, together with the synergistic effects of the finely dispersed smaller bimetallic PtRu nanoparticles, makes this material one of the most active catalysts for the selective hydrogenolysis of HMF to 1,6-HDO.

Received 28th October 2025,  
Accepted 29th October 2025

DOI: 10.1039/d5cy01286d

rsc.li/catalysis

## Introduction

The conversion of 5-hydroxymethylfurfural (HMF) to 1,6-hexanediol (1,6-HDO) through ring-opening hydrogenolysis over supported metal nanoparticle based heterogeneous catalysts represents a promising pathway for producing valuable chemicals from renewable resources.<sup>1-4</sup> The U.S. Department of Energy (DOE) has identified HMF as one of twelve renewable platform molecules, highlighting its potential as a precursor for 1,6-HDO production.<sup>2,5</sup> A few commercial processes for the conversion of lignocellulosic biomass to HMF are being developed.<sup>3,4,6</sup> The presence of two terminal hydroxyl groups in 1,6-HDO makes it particularly valuable as a monomer in polymer synthesis and it is used in

the production of polyesters for polyurethane elastomers, coatings, adhesives and polymeric plasticizers.<sup>7,8</sup> It has also been reported as a key intermediate in the production of caprolactone, a precursor to produce caprolactam, from renewable HMF.<sup>9</sup> Polymers derived from 1,6-HDO exhibit superior properties, including better mechanical strength, low glass transition temperature, and high heat resistance.<sup>8</sup> These characteristics, combined with minimal environmental impact, make 1,6-HDO an important intermediate in polymer manufacturing.<sup>10,11</sup> Current industrial production of 1,6-HDO relies on the catalytic reduction of adipic acid using homogeneous cobalt catalysts.<sup>7</sup> However, this conventional route presents several challenges, including sub-optimal yields and dependence on fossil fuel-derived feedstocks such as cyclohexane and cyclohexene.<sup>10</sup> Recent research has increasingly focused on developing sustainable synthesis routes for 1,6-HDO using renewable biomass feedstocks.<sup>1,12,13</sup> This alternative approach offers numerous advantages and has received considerable attention among researchers.<sup>10,14</sup>

Two pathways exist for converting HMF to 1,6-HDO from HMF. The first pathway is a direct one-pot synthesis, where

<sup>a</sup> Cardiff Catalysis Institute, Translational Research Hub, School of Chemistry, Cardiff University, Cardiff, CF24 4HQ, UK. E-mail: sankar@cardiff.ac.uk

<sup>b</sup> Chemistry Department, Faculty of Science, Taibah University, Al-Madinah Al-Munawarah, 41477, Saudi Arabia

<sup>c</sup> KAUST Catalysis Center (KCC), King Abdullah University of Science and Technology, Thuwal 23955-6900, Saudi Arabia



the C–O bond in the furan ring is broken *via* hydrogenolysis, followed by the hydrogenation of C=O and C=C bonds in the resultant product.<sup>13</sup> These reactions are catalysed by the acidic and metallic sites of the catalysts respectively, hence multi-functional catalysts are required for this reaction.<sup>15</sup> The second pathway proceeds via the initial hydrogenation of HMF to 2,5-dihydroxymethyl tetrahydrofuran (DHMTHF), which subsequently undergoes ring-opening hydrogenolysis to produce 1,6-HDO.<sup>16</sup> The selective one-pot direct hydrogenation/hydrogenolysis of HMF to 1,6-HDO presents significant challenges due to the presence of multiple reactive functionalities including hydroxyl, aldehyde, and C=C groups in HMF. This transformation can potentially yield various products, including 2,5-dihydroxymethylfuran (DHMF), 2,5-dihydroxymethyl tetrahydrofuran (DHMTHF), 1,6-hexanediol (1,6-HDO), and 1,2,6-hexanetriol (1,2,6-HTO), as illustrated in Scheme 1.<sup>9,10,14,17,18</sup> Given these complexities, the development of effective heterogeneous catalysts, that selectively convert HMF to 1,6-HDO, represents both an academic challenge and an industrial priority. Success in this endeavor requires precise control over reaction pathways to achieve high selectivity toward 1,6-HDO while minimizing the formation of undesired byproducts.

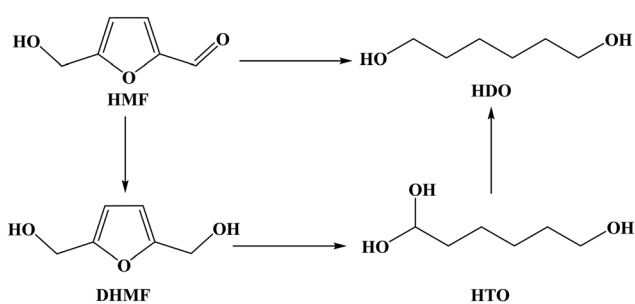
Several supported noble metal nanoparticle-based catalysts have been reported for the ring-opening of HMF to produce diols and triols.<sup>10,19–22</sup> The direct ring opening transformation of HMF was reported over a mixture of copper chromate and Pd/C catalysts under harsh reaction conditions (270 °C, 150 bar) using gaseous H<sub>2</sub> as the reductant, yielding moderate amounts of triols and diols (~4%).<sup>23</sup> Huber and co-workers demonstrated the role of Brønsted acid sites on a Pt–WO<sub>x</sub>/TiO<sub>2</sub> catalyst in the ring-opening of tetrahydrofuran-dimethanol (THFDM) to 1,6-HDO, achieving yields of up to 70%.<sup>24</sup> Xiao and co-workers utilized a dual-layered Pd/SiO<sub>2</sub> and Ir-ReO<sub>x</sub>/SiO<sub>2</sub> system in a fixed-bed reactor to convert HMF to 1,6-HDO at 100 °C and 70 bar H<sub>2</sub>, achieving a 19% yield. They further highlighted the critical role of acid sites in facilitating this transformation.<sup>15</sup> Tuteja and co-workers

reported a 43% yield of 1,6-HDO via catalytic transfer hydrogenation of HMF at 140 °C using formic acid as the hydrogen source over a Pd/ZrP catalyst. As with other catalytic systems, the acidity of the support was found to be pivotal for the ring-opening reaction.<sup>13</sup> Non-noble metal catalysts, such as nickel and copper oxides, have also been employed to convert HMF to products such as 1,2,6-hexanetriol and 1,2-hexanediol under relatively harsh reaction conditions, achieving moderate yields.<sup>18,25</sup> Across most reported catalytic systems, the presence of metallic sites to activate hydrogen, along with acidic and basic sites on the support, has been shown to play a critical role in the ring-opening process. Basic sites promote the adsorption of C=O and C–O–C bonds within the furan ring, while acid sites are essential for the cleavage of the furanic C–O–C bond *via* hydrogenolysis.<sup>25,13,24</sup>

Supported bimetallic nanoparticle-based catalysts have been reported to exhibit higher activity, selectivity, and stability compared to their monometallic counterparts for a variety of reactions, including oxidation, direct synthesis of hydrogen peroxide, hydrogenation/hydrogenolysis and more.<sup>26–30</sup> The catalytic properties of bimetallic nanoparticles can be precisely tuned by controlling their particle size, composition and nanostructure.<sup>31,32</sup> We have reported several supported bimetallic catalysts that outperform their monometallic counterparts during hydrogenation of levulinic acid to gamma-valerolactone,<sup>33</sup> the hydrogenolysis of glycerol to propanediols,<sup>34</sup> and the hydrogenation of CO<sub>2</sub> to formic acid.<sup>35</sup> Hydroxyapatite (HAP), HCa<sub>5</sub>O<sub>13</sub>P<sub>3</sub>, is a versatile support material with both acidic and basic sites and it can also exchange and stabilize a wide variety of metal ions. Importantly, the acidic and basic sites of HAP can be tailored by tuning its bulk Ca/P ratio.<sup>36</sup> For instance, at a lower Ca/P ratio (*ca.* 1.50) HAP is acidic, whilst it is basic at a higher Ca/P ratio (*ca.* 1.67).<sup>37–39</sup> A study by Tsuchida and co-workers<sup>38</sup> suggests that the ratio of Ca/P of HAP influences the distribution of acid sites and basic sites on the catalyst surface with Ca<sup>2+</sup> ions acting as Lewis acid sites, O atoms in PO<sub>4</sub><sup>3–</sup> and OH groups acting as Lewis base sites, and the PO–H as Brønsted acid sites.<sup>37,40–42</sup> The objective of this article is to exploit these properties and develop HAP supported Pt-based heterogeneous catalysts for the conversion of HMF to 1,6-hexanediol at relatively moderate reaction conditions.

## Experimental

All chemicals used in this work were purchased from commercial sources and used without further purification. RuCl<sub>3</sub>·xH<sub>2</sub>O (Sigma Aldrich, 99.9 %), NH<sub>4</sub>ReO<sub>4</sub> (Sigma Aldrich, 99 %), Co(NO<sub>3</sub>)<sub>2</sub> (Sigma Aldrich, 99 %), PdCl<sub>2</sub> (Sigma Aldrich, 99.9 %), H<sub>2</sub>PtCl<sub>6</sub> (Sigma Aldrich, 99.9 %), hydroxyapatite (Acros Organics), hydroxymethyl furfural (Sigma Aldrich, 99%), propylbenzene (Sigma Aldrich, 99%), methanol (Sigma Aldrich, 99.5%).



**Scheme 1** Schematic representation of the conversion of HMF to 1,6-hexanediol over supported metal nanoparticles. HMF: 5-hydroxymethylfurfural; DHMF: 2,5-dihydroxymethylfurfural; HTO: 1,1,6-hexanetriol; and HDO: 1,6-hexanediol. Other intermediate products have been omitted for clarity.



## Catalyst synthesis

Supported monometallic and bimetallic catalysts were synthesized via the wet impregnation method, using aqueous solutions of  $\text{H}_2\text{PtCl}_6$  (18.57 mg<sub>Pt</sub> mL<sup>-1</sup>),  $\text{Co}(\text{NO}_3)_2$  (10.05 mg<sub>Co</sub> mL<sup>-1</sup>),  $\text{NH}_4\text{ReO}_4$  (12.25 mg<sub>Re</sub> mL<sup>-1</sup>),  $\text{PdCl}_2$  (5.53 mg<sub>Pd</sub> mL<sup>-1</sup>) and  $\text{RuCl}_3 \cdot \text{xH}_2\text{O}$  (14.70 mg<sub>Ru</sub> mL<sup>-1</sup>) as metal precursors. The total metal content for all the monometallic and bimetallic catalysts are 5 wt%. A detailed synthesis procedure is reported elsewhere.<sup>34,35,43</sup> Briefly, the required volumes of metal precursor solutions were added to a 50 mL round-bottom flask containing deionized water, and the total volume was adjusted to 16 mL. For the preparation of supported bimetallic catalysts, with equimolar amounts of the two metals, corresponding volumes of the precursor solutions were added. The flask was placed in an oil bath maintained at 60 °C and stirred at 1000 rpm using a magnetic stirrer bar. The solution was stirred vigorously for 10 minutes to ensure homogeneity. Subsequently, an accurately weighed amount of the support material was gradually added over a period of 10 minutes period, under constant stirring at 1000 rpm. The resulting slurry was stirred for an additional 15 minutes at 60 °C. After this, the temperature of the oil bath was increased to 95 °C to evaporate the water. The mixture was held at this temperature for 16 h to ensure complete evaporation. The resulting dried solid was collected and ground thoroughly using a mortar and pestle to obtain a homogeneous powder. A 1 g portion of this dried sample was reduced in a tubular furnace at 450 °C for 4 h under a constant flow of 5%  $\text{H}_2/\text{Ar}$ , with a heating ramp rate of 10 °C min<sup>-1</sup>.

### Ring opening hydrogenolysis of 5-hydroxymethyl furfural

Hydrogenation of HMF was performed in a high-pressure stainless-steel autoclave reactor (50 mL, Parr Instruments, Model 5500HP) equipped with a PTFE liner and an overhead stirrer. The liner was charged with HMF (1.59 mmol), methanol (20 mL) and the required amount of the catalyst (mol<sub>HMF</sub>/mol<sub>metal</sub> = 155). The reactor was purged sequentially with  $\text{N}_2$  (3 times) followed by  $\text{H}_2$  (3 times). Subsequently, the reactor was pressurized to 2 MPa with  $\text{H}_2$  and heated to the desired reaction temperature with a constant stirring speed of 1000 rpm. Upon completion of the reaction, stirring was stopped, and the reactor was cooled in an ice bath for 15 min to bring the reactor temperature to approximately 5 °C, ensuring complete cooling of both the reactor and the reaction mixture. The reactor was then depressurized and opened, and the solid catalyst was separated from the reaction mixture using a 0.45 μm PTFE syringe filter. For quantitative analysis, a 10 mL aliquot of the reaction mixture was combined with 0.1 mL of propylbenzene (external standard) and transferred to a GC vial and analysed by GC. For this, Bruker scion 456-GC fitted with a RESTEK Rtx®-1 column (60 m, 0.32 mm ID) and a flame ionization detector (FID) was used with  $\text{N}_2$  carrier gas. To evaluate catalyst reusability, hydrogenation reactions were conducted under

identical reaction conditions across multiple cycles. Following each run, the solid catalyst was recovered by centrifugation, then washed three times with methanol and once with acetone. The catalyst was air-dried overnight at 21 °C, followed by further drying at 110 °C in static air for 10 minutes in an oven prior to reuse. To ensure a consistent catalyst mass in each cycle, two parallel reactions were carried out under identical conditions, and the recovered catalyst from both was combined for subsequent use. Catalytic performance was monitored across successive cycles to assess reusability.

### Catalyst characterization

**X-ray photoelectron spectroscopy (XPS).** Catalysts were investigated using X-ray photoelectron spectroscopy (XPS) using a Kratos Axis Ultra DLD system (Manchester, UK). Data were collected using monochromatic Al Ka X-ray source (photon energy = 1486.6 eV) operating at 120 W (10 mA × 12 kV), with pass energies of 160 eV for survey spectra, and 40 eV for the high-resolution scans with step sizes of 1 eV and 0.1 eV respectively. The system was operated in the Hybrid mode, using a combination of magnetic immersion and electrostatic lenses, and acquired over an area approximately 300 × 700 μm<sup>2</sup>. A magnetically confined charge compensation system using low energy electrons was used to minimize charging of the sample surface, and all spectra were taken with a 90° take-off angle. A pressure of *ca.* 5 × 10<sup>-9</sup> Torr was maintained during collection of the spectra. All samples were pressed onto silicone free double sided adhesive tape attached to an iso-propyl alcohol cleaned cut glass microscope slide to ensure electrical isolation from the spectrometer. All data was analysed using CasaXPS (v2.3.26)<sup>44</sup> after subtraction of a Shirley background and using modified Wagner sensitivity factors as supplied by the instrument manufacturer. Where required, curve fits were performed using an asymmetric Lorentzian form (LA lineshape in CasaXPS) and peak models derived using model compounds recorded under identical conditions. Binding energies are quoted with an uncertainty of ±0.2 eV, due to the uncertainty of the C(1s) calibration, taken to be 284.8 eV.

**Scanning transmission electron microscopy (STEM).** STEM was used to determine the particle size distribution of the monometallic and bimetallic catalysts. To prepare the samples for STEM analysis, they were dispersed in ethanol by ultrasonication and then deposited on copper grids which had been coated with holey carbon film, the grid was cleaned with a plasma cleaner. HAADF-STEM measurements were carried out using a Thermo Fisher Scientific Titan Cs Probe microscope operating at a beam current of 0.35 nA.

**Inductively coupled plasma-mass spectrometry (ICP-MS).** Inductively Coupled Plasma Mass Spectrometry (ICP-MS) was used for the quantitative analysis of the elements. Analyses were carried out using the Agilent Technologies 7900 ICP-MS system fitted with an Agilent Integrated Autosampler.



Quantitative data were obtained using internal standards and standard calibration plots.

**Temperature Programmed Desorption (TPD).** Temperature programmed desorption of ammonia ( $\text{NH}_3$ -TPD) was performed using the Micro-activity Reference setup (PID Eng&Tech). 100 mg of the supported monometallic and bimetallic catalysts were placed in a fixed bed quartz tube reactor. The concentrations of inlet and outlet of  $\text{NH}_3$  were monitored and controlled using MultiGasTM 2030 FT-IR continuous gas analyzer. The catalyst samples were pretreated under  $\text{N}_2$  at 400 °C for 2 h (ramp rate 5 °C min<sup>-1</sup>). After cooling down to 100 °C, the sample was exposed to 1100 ppm of  $\text{NH}_3$  flow for 1 h (total flow 200 ml min<sup>-1</sup>). The physisorbed  $\text{NH}_3$  was removed by purging the catalysts with 200 mL min<sup>-1</sup> of  $\text{N}_2$  flow for 60 min. Finally, the desorption of  $\text{NH}_3$  was performed by increasing the temperature from 100 to 600 °C (ramp rate 5 °C min<sup>-1</sup>). Temperature programmed desorption of carbon dioxide ( $\text{CO}_2$ -TPD) was performed using the Autochem 2920 system (Micromeritics Instruments Co.). 100 mg of the supported monometallic and bimetallic samples were pretreated at 400 °C for 2 h under  $\text{N}_2$  flow. The sample was cooled down to 50 °C and exposed to  $\text{CO}_2$  adsorption for 1 h. The saturated sample was flushed with He for 1 h to remove physisorbed  $\text{CO}_2$ , and then the temperature was increased to 600 °C with a heating ramp of 5 °C min<sup>-1</sup>.

## Results and discussion

The acidic and basic properties of catalyst support materials play a crucial role in the ring-opening hydrogenolysis of 5-hydroxymethylfurfural (HMF) towards 1,6-hexanediol (1,6-HDO). To systematically investigate this influence, a series of 5 wt% supported platinum catalysts were prepared *via* the wet impregnation, using cerium dioxide ( $\text{CeO}_2$ ), magnesium oxide ( $\text{MgO}$ ), hydrotalcite (HT), and hydroxyapatite (HAP) as supports. The catalytic activity of these materials was

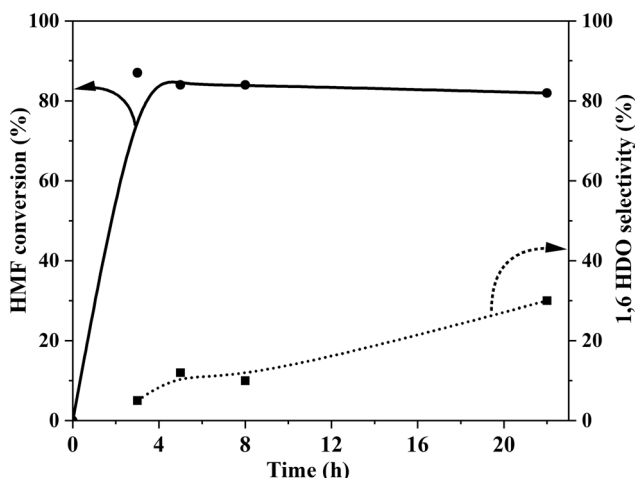


Fig. 1 Time on line catalytic data for the ring opening hydrogenolysis of HMF to 1,6-HDO over monometallic 5% Pt/HAP. Reaction conditions: HMF: 1.59 mmol; HMF/Pt molar ratio: 155; methanol: 20 mL;  $\text{H}_2$ : 2 MPa; temperature: 120 °C; stirring: 1000 rpm.

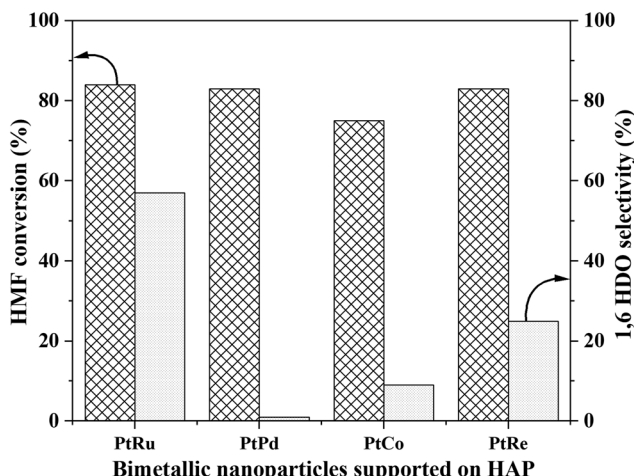


Fig. 2 Comparison of the catalytic activities of different bimetallic nanoparticles (5wt%) supported on HAP for the ring opening hydrogenolysis of HMF to 1,6-HDO. Reaction conditions: HMF: 1.59 mmol; HMF/total metal molar ratio: 155; methanol: 20 mL;  $\text{H}_2$ : 2 MPa; temperature: 120 °C; stirring: 1000 rpm; time: 8 h.

evaluated for HMF hydrogenation under batch autoclave conditions at 120 °C and 2 MPa  $\text{H}_2$  for 5 h (SI, Fig. S1). Among the tested catalysts, 5 wt% Pt/HAP showed a 88% HMF conversion but exhibited a relatively low 1,6-HDO selectivity of 13%. However, Pt nanoparticles supported on  $\text{CeO}_2$ ,  $\text{MgO}$ , and HT produced 2,5-dihydroxymethylfurfural (DHMF) with relatively high selectivity. It is important to note that these catalysts did not produce any 1,6-HDO. In particular, 5 wt% Pt/MgO achieved a remarkable >99% HMF conversion with >99% selectivity towards DHMF. Since the primary objective of this study is to produce 1,6-HDO, we did not study this promising catalyst further. To further understand the reaction kinetics of 5 wt% Pt/HAP, the

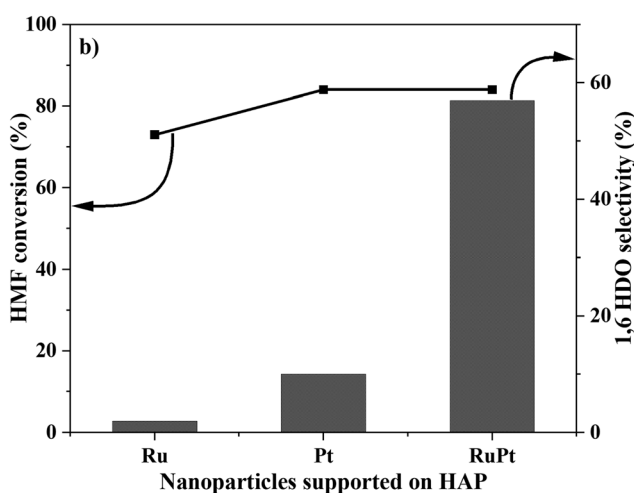


Fig. 3 Comparison of the catalytic activities of monometallic and bimetallic nanoparticles (5%) supported on HAP for the ring opening hydrogenolysis of HMF to 1,6-HDO. Reaction conditions: HMF: 1.59 mmol; HMF/metal molar ratio: 155; Methanol: 20 mL;  $\text{H}_2$ : 2 MPa; temperature: 120 °C; stirring: 1000 rpm; time: 8 h.



catalytic activity was monitored as a function of time (Fig. 1). The HMF conversion increased steadily, reaching approximately 87% within the first 3 h, and subsequently remained relatively constant (85%) up to 22 h. However, the selectivity towards 1,6-HDO displayed a gradual increase from 5% after 3 h to 30% after 22 h, accompanied by a corresponding decrease in DHMF selectivity (data not shown in Fig. 1 for clarity). Gas chromatography (GC) and gas chromatography-mass spectrometry (GC-MS) analyses of the reaction mixture identified further products including methylfurfural (MF) and dimethylfuran (DMF) as additional byproducts in the reaction mixture. There were some unidentified products present in the reaction mixture, however their selectivities were typically <10%.

The 5 wt% Pt/HAP catalyst demonstrated a higher or comparable 1,6-HDO yield from HMF hydrogenation compared to previously reported heterogeneous catalysts (Table S1, SI). However, the selectivity towards 1,6-HDO was less (*ca.* 30%). To address this, a series of bimetallic PtM/HAP catalysts (where M = Co, Ru, Pd, or Re) were synthesized and evaluated for HMF conversion to 1,6-HDO (Fig. 2). Notably, the bimetallic PtRu/HAP catalyst exhibited remarkable activity, maintaining HMF conversion rates comparable to the monometallic Pt catalyst while substantially increasing the 1,6-HDO selectivity from 30% for the monometallic Pt catalyst to 57% for the bimetallic PtRu/HAP catalyst (Fig. 2). To elucidate the role of ruthenium in this selectivity enhancement, a monometallic 5%Ru/HAP catalyst was also synthesized and tested (Fig. 3). This catalyst displayed negligible 1,6-HDO selectivity (2%), confirming the synergistic effect between Pt and Ru within the bimetallic RuPt system. This is the first report of a supported bimetallic catalyst exhibiting superior catalytic activity towards the ring-opening hydrogenolysis of HMF to 1,6-HDO, compared to the constituent monometallic catalysts. However, the efficacy of

bimetallic catalysts varied significantly. The PtCo and PtPd catalysts gave lower 1,6-HDO selectivities (9% and 1%, respectively) compared to the monometallic Pt catalyst. Conversely, the PtRe/HAP catalyst exhibited a 1,6-HDO selectivity (*ca.* 25%) which is similar to the monometallic Pt catalyst, suggesting that the incorporation of Re did not substantially alter the catalytic behaviour (Fig. 2). To gain further insights into the performance of the bimetallic PtRu/HAP catalyst, its catalytic activity was evaluated as a function of reaction time (Fig. 4). HMF conversion gradually increased, reaching *ca.* 80% after 3 h, and remained stable until 23 h – a trend also observed for the monometallic Pt/HAP catalyst. However, the selectivity towards 1,6-HDO over PtRu/HAP increased steadily, reaching 62% after 15 h, after which no significant increase was observed. For clarity, only HMF conversion and 1,6-HDO selectivity are provided in the plot. A plot containing the selectivities of all the products are given in the supported information (Fig. S2). A few unidentified products were also observed, however their selectivities were <5%. The carbon balance for a representative reaction is found to be >60%. This is mainly because of unidentified products and other side reactions including polymerisation of HMF and reaction with the solvent. The observed stabilization in both conversion and selectivity beyond specific time points suggests possible catalyst deactivation, prompting further investigation through reusability studies.

Reusability experiments were performed to assess the stability of the PtRu/HAP catalyst during the hydrogenation of HMF under 20 bar H<sub>2</sub> pressure at 120 °C for 2 hours. After each cycle, the catalyst was recovered, washed and dried and reused under identical reaction conditions. The PtRu/HAP catalyst showed nearly stable performance over three consecutive cycles, consistently achieving ~84% HMF conversion and ~6% selectivity toward 1,6-HDO (Fig. 5). This stability suggests that the observed activity plateauing is not attributable to catalyst deactivation, underscoring the

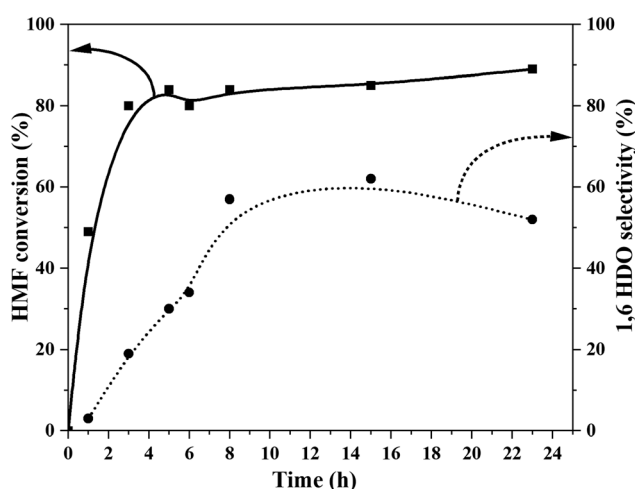


Fig. 4 Time on line data for the ring opening hydrogenolysis of HMF to 1,6-HDO over bimetallic 5% PtRu/HAP. Reaction conditions: HMF: 1.59 mmol; HMF/Total metal molar ratio: 155; methanol: 20 mL; H<sub>2</sub>: 2 MPa; temperature: 120 °C; stirring: 1000 rpm.

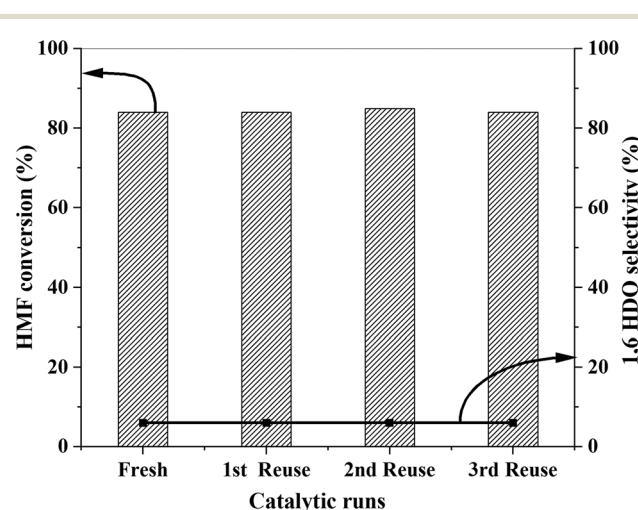
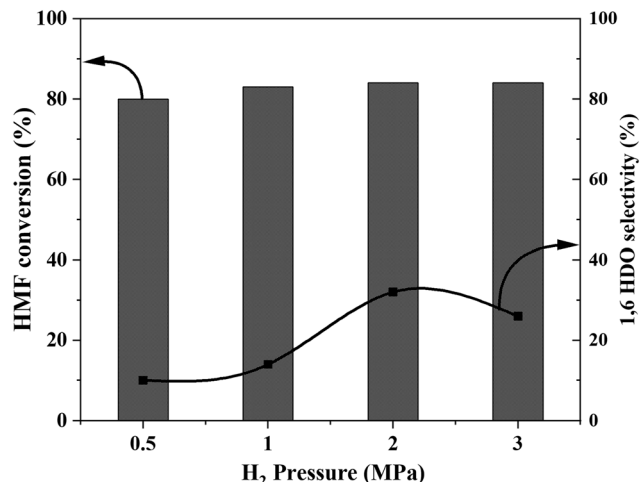


Fig. 5 Reusability of 5% PtRu/HAP catalyst. Reaction conditions: HMF: 1.59 mmol; HMF/Pt molar ratio: 155; methanol: 20 mL; H<sub>2</sub>: 2 MPa; temperature: 120 °C; stirring: 1000 rpm; time: 2h.





**Fig. 6** Effect of the hydrogen pressure during the ring opening hydrogenolysis of HMF over 5% RuPt/HAP. Reaction conditions: HMF: 1.59 mmol; methanol: 20 mL; temperature: 120 °C; time: 5 h; HMF/total metal molar ratio: 155.

stability of the PtRu/HAP system under the reaction conditions. Further investigation is required to elucidate the underlying reason behind the activity and selectivity plateauing.

The influence of reaction conditions on the hydrogenation of HMF to 1,6-HDO was investigated using the bimetallic 5 wt.% PtRu/HAP catalyst, with a focus on assessing the effects on HMF conversion and 1,6-HDO selectivity. Specifically, the impact of hydrogen pressure was studied at 0.5, 1, 2, and 3 MPa, with reactions conducted for 5 h at 120 °C. The corresponding results are shown in Fig. 6. HMF conversion remained consistently high (~80%) across all tested H<sub>2</sub> pressures with a moderate increase in the conversion with the increase in H<sub>2</sub> pressure (from 80% to 84%). In contrast, selectivity toward 1,6-HDO exhibited a pressure-dependent

trend. At 0.5 MPa, the selectivity was 10%, increasing to 14% and 32% at 1 MPa and 2 MPa, respectively. Notably, a further increase in pressure to 3 MPa resulted in a decline in 1,6-HDO selectivity to 26%. This trend suggests that increasing H<sub>2</sub> pressure initially enhances the hydrogenolysis step, likely due to a higher concentration of dissolved hydrogen in methanol, which improves surface hydrogen coverage on the metal catalyst and promotes the desired reaction pathway. However, at pressures exceeding 2 MPa, the decline in selectivity may be attributed to the formation of oligomeric by-products, which can occur under high hydrogen pressures *via* secondary reactions involving hydrogenated intermediates.<sup>47,48</sup>

Reaction temperature is a critical parameter influencing both the conversion of HMF and the selectivity toward 1,6-HDO in the hydrogenation process. To investigate this effect, reactions were conducted at temperatures ranging from 80 to 160 °C using a 5 wt% PtRu/HAP catalyst under 2 MPa hydrogen pressure for 5 h. The results, presented in Fig. 7, show that temperature has a significant impact on both catalyst performance and product distribution.

At 80 °C, despite achieving a high HMF conversion of 93%, 1,6-HDO was not detected, with 2,5-dimethylfuran (DMHF) identified as the primary product. In the temperature range of 100–140 °C, selectivity toward 1,6-HDO increased progressively with temperature. At 100 °C, DMHF remained the dominant product, and the selectivity toward 1,6-HDO was limited to 2%. Increasing the temperature to 120 °C resulted in a notable rise in 1,6-HDO selectivity to 32%, with a corresponding HMF conversion of 84%. At 140 °C, the selectivity further increased to 51%, accompanied by a 90% conversion. Raising the temperature to 160 °C led to complete HMF conversion (100%), while the 1,6-HDO selectivity remained essentially unchanged.

The enhancement in 1,6-HDO selectivity with increasing temperature—despite comparable HMF conversions—suggests that the ring-opening step leading to 1,6-HDO formation has a higher activation energy than the initial hydrogenation of HMF. This observation aligns with results from theoretical studies on furan hydrogenation over Pd(111) surfaces.<sup>45</sup> Further optimisation studies are needed to maximise 1,6-HDO yield.

### Catalyst characterization

To elucidate the relationship between the observed catalytic behavior and the physicochemical properties of monometallic and bimetallic nanoparticles as well as their supports, all catalysts were comprehensively characterized using X-ray photoelectron spectroscopy (XPS) and scanning transmission electron microscopy (STEM). XPS was employed to investigate the chemical states of the metal components in both fresh and spent monometallic and bimetallic catalysts, providing insights into potential changes induced during catalytic reactions.

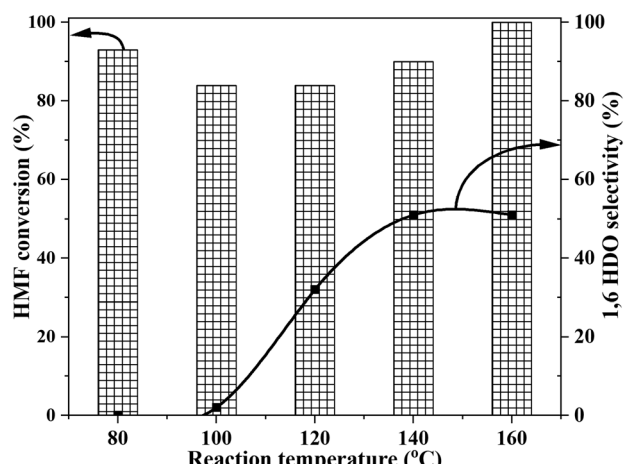


**Fig. 7** Effect of reaction temperature during the ring opening hydrogenolysis of HMF over 5% RuPt/HAP. Reaction conditions: HMF: 1.59 mmol; methanol: 20 mL; H<sub>2</sub> pressure: 2 MPa; time: 5 h; HMF/total metal molar ratio: 155.



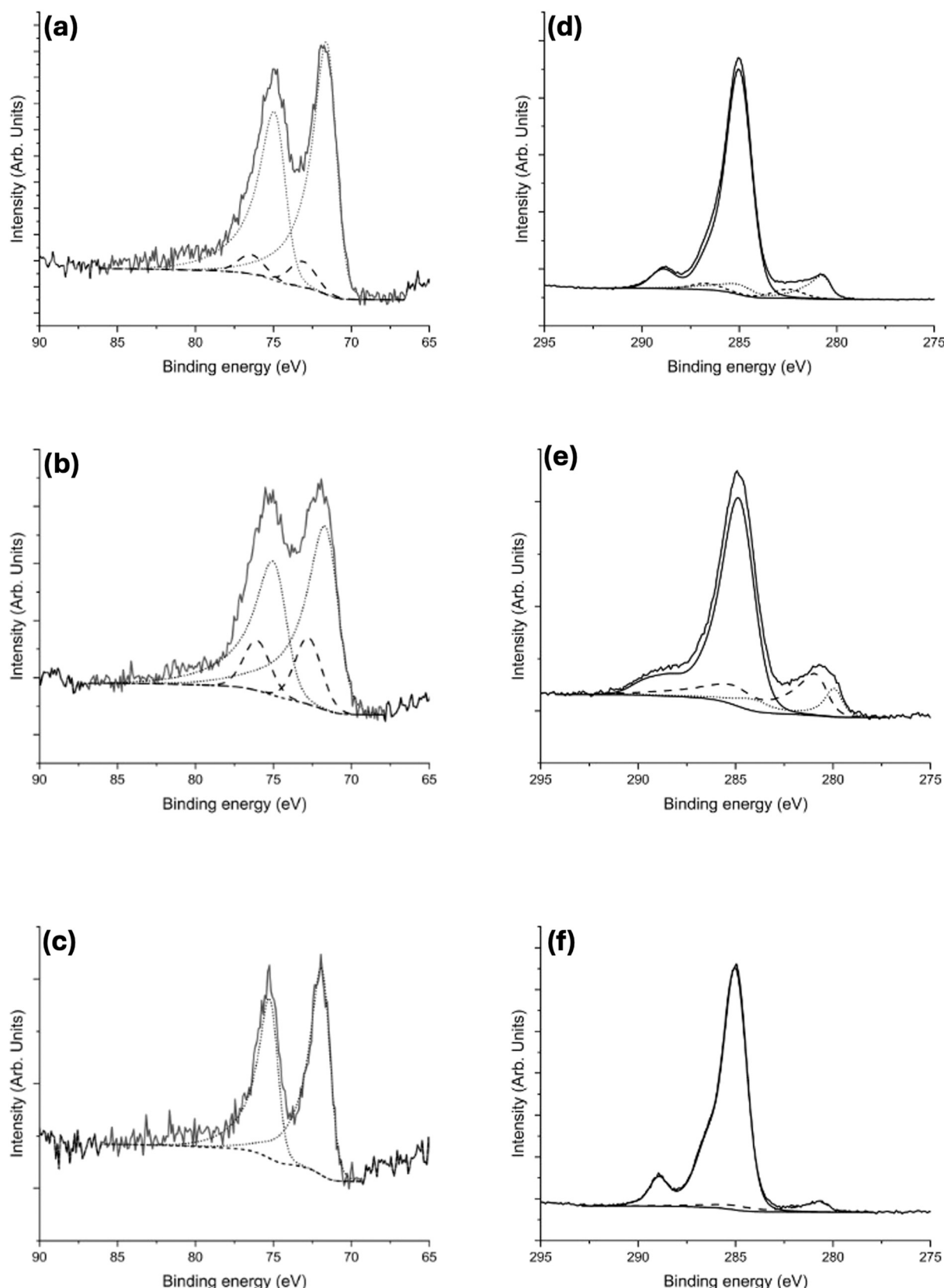


**Fig. 8** XPS spectra of the monometallic and bimetallic catalysts: fitted Pt(4f) spectra of (a) fresh monometallic 5% Pt/HAP; fresh bimetallic 5% PtRu/HAP (b); spent bimetallic 5% PtRu/HAP (c); XPS fitted Ru(3d) spectra of fresh monometallic 5% Pt/HAP (d); fresh bimetallic 5% PtRu/HAP (e) and spent bimetallic 5% PtRu/HAP (f). Note for clarity, due to overlap of the Ru(3d) signal with the C(1s) signal, the fitted spectra are plotted as the sum of all the components for each chemical species (Ru(0), Ru(IV) and C(1s)). For the metals, solid lines represent the zero valence state, where as dashed lines represent the oxidized state as discussed in the text.



As shown in Fig. 8(a and b) XPS analysis of fresh Pt and PtRu/HAP catalysts exhibit a characteristic asymmetric shape and Pt(4f<sub>7/2</sub>) binding energies of 71.5 eV, consistent with metallic Pt,<sup>34,46</sup> a smaller higher binding energy Pt species is noted, as is the case for the bimetallic PtRu/HAP catalysts, the energy of which is 72.7 eV. Since both Pt and Ru have similar electronegativities (2.20 for Ru and 2.28 for Pt) this higher binding energy could be because of a different species such as Pt(OH)<sub>2</sub> or PtO.<sup>47</sup>

The monometallic Ru and bimetallic PtRu catalysts Fig. 8(d and e) reveal differences of the Ru chemistry. For the monometallic, Ru is found predominantly as hydrated RuO<sub>2</sub> as evidenced by the asymmetric peak centred at 280.8 eV,

with some residual Ru-Cl species at *ca.* 282.5 eV, whilst the bimetallic catalyst, exhibits both metallic Ru (279.9 eV) and RuO<sub>2</sub>.<sup>48</sup> We attribute the hydrated Ru and Pt species to air handling of the reduced materials.

After use, the bimetallic catalyst exhibits a single oxidation state for each metal; specifically metallic Pt (Fig. 8c) and RuO<sub>2</sub> (Fig. 8e). A shift to higher value for the Pt(4f) binding energy is noted by *ca.* 0.4 eV, and likely attributable to a smaller particle size as noted by STEM.

Scanning Transmission Electron Microscopy (STEM) was employed to investigate the particle size distributions of the monometallic Pt/HAP, Ru/HAP, and bimetallic PtRu/HAP catalysts. Representative STEM images and corresponding

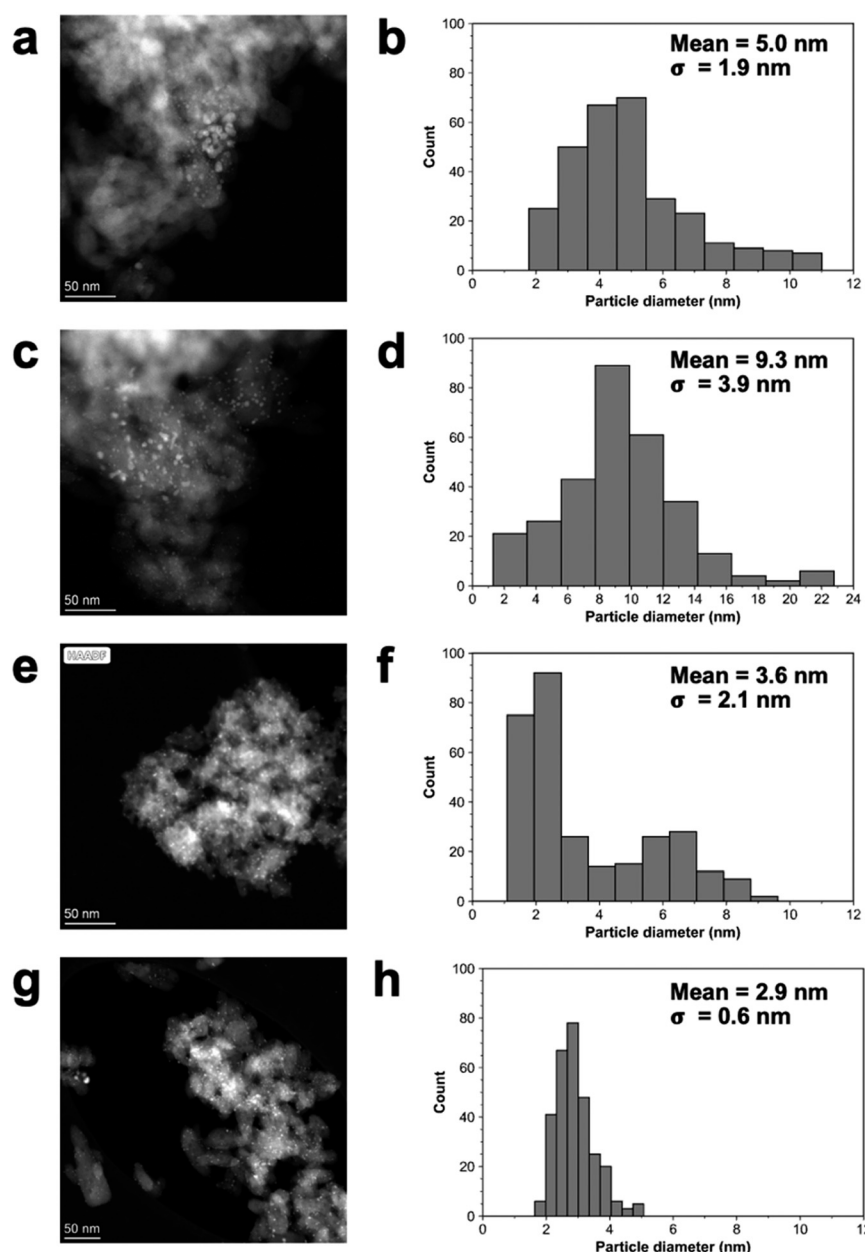


**Fig. 9** STEM images and particle size distribution of (a + b) 5 wt% Ru/HAP; (c + d) wt% Pt/HAP; (e + f) 5 wt% PtRu/HAP; (g + h) 5 wt% PtRu/HAP spent catalyst.



Table 1 Quantitative analyses of the Ca/P ratio using XPS and ICP-MS and the basic sites using CO<sub>2</sub> TPD

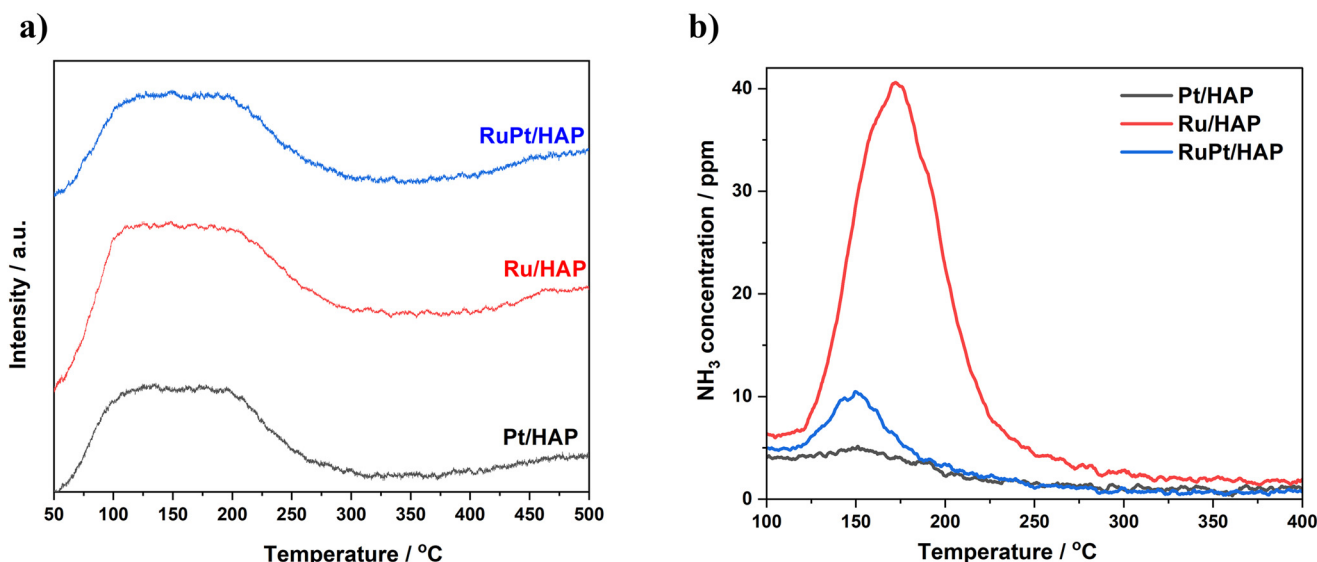
Ca/P molar ratio <sup>b</sup>	Ca/P molar ratio <sup>a</sup>	Catalyst	Amount of basic sites <sup>c</sup> (mmol g <sup>-1</sup> )		
			Total	Peak 2 (temp °C)	Peak 1 (temp °C)
Pt/HAP	1.61	1.59	0.225(136)	0.079(552)	0.304
Ru/HAP	1.45	1.57	0.338(110)	0.058(510)	0.396
PtRu/HAP	1.50	1.57	0.215(149)	0.062(499)	0.277

<sup>a</sup> From XPS analyses. <sup>b</sup> From ICP-MS analyses. <sup>c</sup> From CO<sub>2</sub> TPD.

particle size distributions are presented in Fig. 9. The monometallic Ru/HAP and Pt/HAP catalysts exhibited average particle sizes of  $5.0 \pm 1.9$  nm and  $9.3 \pm 3.9$  nm, respectively, whereas the bimetallic PtRu/HAP catalyst displayed a smaller average particle size of  $3.6 \pm 2.1$  nm. This reduction in particle size upon incorporation of Ru into Pt nanoparticles suggests an enhanced stabilization effect, likely attributable to the presence of Ru. Previous work by our group on bimetallic PdRu catalysts synthesized using the same methodology confirmed the formation of homogeneous random alloy structures.<sup>28,33</sup> Based on these earlier findings, it is reasonable to infer that the PtRu/HAP catalysts investigated in the present study also exhibit a homogeneous random alloy structure. Because of this homogeneous random alloy structure, it is not possible to quantify the particle sizes of individual atoms. The combination of this structural homogeneity with the smaller particle size could be the reason for the observed synergistic enhancements in catalytic performance. Further STEM analysis was conducted on the spent PtRu/HAP catalyst, as shown in Fig. 9g and h. Notably, the particle size remained largely unchanged after the reaction, with the fresh and spent catalysts exhibiting average sizes of 3.6 nm and 2.9 nm, respectively. This observation highlights the excellent structural stability of the bimetallic catalyst under reaction conditions and supports its

demonstrated reusability. The exceptional stability of the PtRu/HAP catalyst may be attributed to strong interactions between the metal nanoparticles and the phosphate groups present on the HAP surface, which are known to facilitate anchoring via electron-donating interactions.

Hydroxyapatite (HAP) belongs to a broad family of isomorphic compounds and is among the most prevalent forms of calcium phosphate.<sup>36,39</sup> It is a non-stoichiometric material, characterized by a variable Ca/P ratio that typically ranges from 1.50 to 1.67. This ratio serves as a well-established indicator of the overall acidic or basic character of HAP. At a Ca/P ratio of 1.50, HAP predominantly exhibits acidic properties while retaining some basic sites. Conversely, at a ratio of 1.67, it functions as a basic catalyst with residual acidic functionality.<sup>36–39</sup> To evaluate the acid-base properties of the supports used in this study, the Ca/P ratios of the monometallic and bimetallic catalysts were determined using both X-ray photoelectron spectroscopy (XPS) and inductively coupled plasma mass spectrometry (ICP-MS), as presented in Table 1. XPS provided insights into the surface Ca/P ratio, while ICP-MS was used to assess the bulk composition. As expected and consistent with previous literature,<sup>36,37,40</sup> the surface Ca/P ratios were found to differ from the bulk values, reflecting the inherent surface heterogeneity of HAP. While the bulk Ca/P ratios remained nearly constant across all three

Fig. 10 Temperature programmed desorption profiles a) CO<sub>2</sub> and b) NH<sub>3</sub> of monometallic and bimetallic nanoparticles supported on HAP.

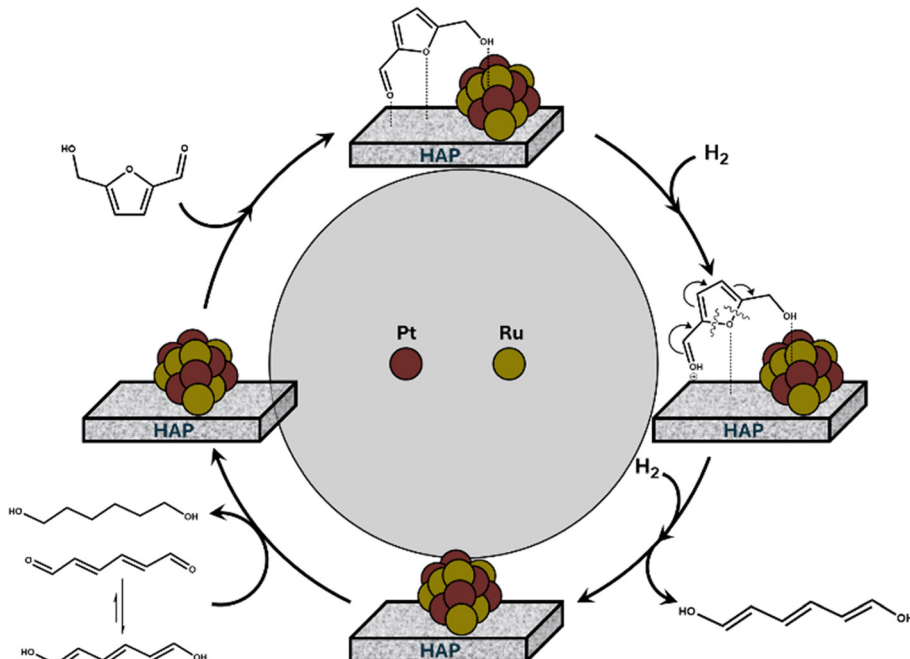


Fig. 11 Proposed mechanism for the conversion of HMF to 1,6-HDO over bimetallic PtRu nanoparticles supported on HAP.

catalysts, notable differences were observed in the surface compositions. The monometallic Pt/HAP catalyst exhibited a surface Ca/P ratio of 1.61, indicating a predominantly basic support with some acidic sites. In contrast, the bimetallic PtRu/HAP catalyst displayed a surface Ca/P ratio of 1.50, characteristic of an acidic support with residual basic functionality. To complement this,  $\text{NH}_3$  TPD and  $\text{CO}_2$  TPD studies were performed on the monometallic and bimetallic catalysts (Fig. 10). Fig. 10a shows the  $\text{CO}_2$  TPD profiles, with all the three catalysts showing two desorption peaks (110–150 °C & 510–550 °C) attributed to two different basic sites with differing strengths. The weaker basic sites are more abundant than the stronger basic sites. The total basic site density follows the sequence Ru/HAP > Pt/HAP > PtRu/HAP. Fig. 10b shows the  $\text{NH}_3$  – TPD data for the three catalysts, where the integrated peak areas indicate the total acidity trend: Ru/HAP > PtRu/HAP > Pt/HAP. The 1,6-HDO yield follows the trend PtRu/HAP > Pt/HAP > Ru/HAP, indicating that the ring-opening hydrogenolysis does not correlate with a single catalyst property. Instead, the combination of optimal balance of acidic and basic sites of HAP and the smaller bimetallic PtRu nanoparticles is responsible for the superior catalytic activity of the bimetallic PtRu/HAP catalyst. The mechanism of this ring opening hydrogenolysis is presented in Fig. 11.

## Conclusions

This study addresses a key challenge in sustainable chemistry: the development of efficient catalytic pathways for the conversion of biomass-derived platform molecules into high-value chemicals. We report the design and evaluation of

supported platinum-based heterogeneous catalysts for the transformation of 5-hydroxymethylfurfural (HMF) to 1,6-hexanediol (1,6-HDO), representing a strategic route toward the production of industrially relevant compounds from renewable resources. Initially, a series of monometallic Pt catalysts supported on cerium oxide ( $\text{CeO}_2$ ), magnesium oxide ( $\text{MgO}$ ), hydrotalcite, and hydroxyapatite (HAP) were investigated. Among these, the Pt/HAP catalyst exhibited the highest performance, achieving a 1,6-HDO selectivity of 27%. This superior activity is attributed to the amphoteric nature of HAP, which provides both acidic and basic active sites that are important for this reaction. To further enhance catalytic performance, bimetallic Pt-based nanoparticles (PtPd, PtCo, PtRu, and PtRe) supported on HAP were synthesized and evaluated. Among them, PtRu/HAP was the most effective catalyst, achieving a notable 1,6-HDO selectivity of 57%—more than double that of the monometallic Pt/HAP catalyst. To elucidate the origin of this enhanced performance, the catalysts were characterized using X-ray photoelectron spectroscopy (XPS), scanning transmission electron microscopy (STEM), and inductively coupled plasma mass spectrometry (ICP-MS). These analyses revealed that the incorporation of Ru into Pt nanoparticles leads to the formation of smaller, more uniformly distributed bimetallic nanoparticles with improved stability, which is a key factor in the observed catalytic enhancement. To study the role of support's surface acidity and basicity, we examined the Ca/P ratio, determined by XPS and ICP-MS, and complemented the data with  $\text{CO}_2$  and  $\text{NH}_3$  TPD analyses. The most active PtRu/HAP catalyst exhibited a surface Ca/P ratio of 1.50, indicating a predominantly acidic support with some basic sites. The  $\text{CO}_2$  TPD data showed that the bimetallic PtRu/

HAP catalyst has the least basic sites density among the three catalysts, whereas the NH<sub>3</sub>-TPD data showed an optimal density of acidic sites. This balanced distribution of acidic and basic sites is key to the efficient ring-opening hydrogenolysis of the furan ring in HMF, thereby promoting the formation of 1,6-HDO. Overall, this work demonstrates a significant advancement in the catalytic upgrading of biomass-derived molecules. By integrating rational catalyst design with detailed physicochemical characterization, we highlight the potential of bimetallic PtRu catalysts supported on hydroxyapatite for the efficient and selective production of value-added chemicals from renewable feedstocks.

## Conflicts of interest

There are no conflicts of interest to declare.

## Data availability

The data supporting this article have been included as part of the supplementary information (SI). Supplementary information is available. See DOI: <https://doi.org/10.1039/d5cy01286d>.

## Acknowledgements

HA thanks the Kingdom of Saudi Arabia and Taibah University for funding her PhD studies. MC and MS acknowledge the funding by the Engineering and Physical Sciences Research Council *via* the Prosperity Partnership EP/V056565/1 with bp and Johnson Matthey plc in collaboration with Cardiff University and the University of Manchester. XPS data collection was performed at the EPSRC National Facility for XPS ("HarwellXPS"), operated by Cardiff University and UCL, under Contract No. PR16195. MC, JRM and MS acknowledges the UK-Saudi challenge fund by the British Council.

## References

- 1 T. Buntara, S. Noel, P. H. Phua, I. Melián-Cabrera, J. G. De Vries and H. J. Heeres, Caprolactam from renewable resources: Catalytic conversion of 5-hydroxymethylfurfural into caprolactone, *Angew. Chem., Int. Ed.*, 2011, **50**(31), 7083–7087.
- 2 G. W. Huber, S. Iborra and A. Corma, Synthesis of Transportation Fuels from Biomass: Chemistry, Catalysts, and Engineering, *Chem. Rev.*, 2006, **106**(9), 4044–4098.
- 3 R.-J. van Putten, J. C. van der Waal, E. de Jong, C. B. Rasrendra, H. J. Heeres and J. G. de Vries, Hydroxymethylfurfural, A Versatile Platform Chemical Made from Renewable Resources, *Chem. Rev.*, 2013, **113**(3), 1499–1597.
- 4 C. Chen, M. Lv, H. Hu, L. Huai, B. Zhu, S. Fan, Q. Wang and J. Zhang, 5-Hydroxymethylfurfural and its Downstream Chemicals: A Review of Catalytic Routes, *Adv. Mater.*, 2024, **36**(37), 2311464.
- 5 T. Werpy and G. Petersen, Top value added chemicals from biomass: volume I—results of screening for potential candidates from sugars and synthesis gas: National Renewable Energy Lab. (NREL), Golden, CO (USA), 2004.
- 6 C. Rosenfeld, J. Konnerth, W. Sailer-Kronlachner, P. Solt, T. Rosenau and H. W. G. van Herwijnen, Current Situation of the Challenging Scale-Up Development of Hydroxymethylfurfural Production, *ChemSusChem*, 2020, **13**(14), 3544–3564.
- 7 P. Werle, M. Morawietz, S. Lundmark, K. Sørensen, E. Karvinen and J. Lehtonen, Alcohols, Polyhydric, *Ullmann's Encyclopedia of Industrial Chemistry*, 2000.
- 8 W. M. K. Siegu, L. D. W. Djounoukep, N. B. S. Selabi, E. M. Bonku, Z. Cheng and M. Gauthier, Synergistic Effect and Structure–Property of Bio-based 1,6-Hexanediol on Thermal, Mechanical and Degradation Properties of Biopolymers, *J. Polym. Environ.*, 2023, **31**(3), 1144–1159.
- 9 T. Buntara, S. Noel, P. H. Phua, I. Melián-Cabrera, J. G. de Vries and H. J. Heeres, Caprolactam from renewable resources: catalytic conversion of 5-hydroxymethylfurfural into caprolactone, *Angew. Chem., Int. Ed.*, 2011, **50**(31), 7083–7087.
- 10 N. Enjamuri and S. Darbha, Solid catalysts for conversion of furfural and its derivatives to alkanediols, *Catal. Rev.: Sci. Eng.*, 2020, **62**(4), 566–606.
- 11 C. Japu, A. Alla, A. Martínez de Ilarduya, M. G. García-Martín, E. Benito, J. A. Galbis and S. Muñoz-Guerra, Bio-based aromatic copolymers made from 1,6-hexanediol and bicyclic diacetalized d-glucitol, *Polym. Chem.*, 2012, **3**(8), 2092–2101.
- 12 T. Buntara, S. Noel, P. H. Phua, I. Melián-Cabrera, J. G. de Vries and H. J. Heeres, From 5-Hydroxymethylfurfural (HMF) to Polymer Precursors: Catalyst Screening Studies on the Conversion of 1,2,6-hexanetriol to 1,6-hexanediol, *Top. Catal.*, 2012, **55**(7), 612–619.
- 13 J. Tuteja, H. Choudhary, S. Nishimura and K. Ebitani, Direct Synthesis of 1,6-Hexanediol from HMF over a Heterogeneous Pd/ZrP Catalyst using Formic Acid as Hydrogen Source, *ChemSusChem*, 2014, **7**(1), 96–100.
- 14 Z. Huang, J. Wang, J. Lei, W. Zhao, H. Chen, Y. Yang, Q. Xu and X. Liu, Recent Advances in the Catalytic Hydroconversion of 5-Hydroxymethylfurfural to Valuable Diols, *Front. Chem.*, 2022, **10**, 925603.
- 15 B. Xiao, M. Zheng, X. Li, J. Pang, R. Sun, H. Wang, X. Pang, A. Wang, X. Wang and T. Zhang, Synthesis of 1,6-hexanediol from HMF over double-layered catalysts of Pd/SiO<sub>2</sub> + Ir-ReO<sub>x</sub>/SiO<sub>2</sub> in a fixed-bed reactor, *Green Chem.*, 2016, **18**(7), 2175–2184.
- 16 M. Faber, Process for Producing Adipic Acid from Biomass, *US Pat.*, US4400468A, 1983, vol. 4(400), p. 468.
- 17 S. H. Krishna, K. Huang, K. J. Barnett, J. He, C. T. Maravelias, J. A. Dumesic, G. W. Huber, M. De bruyn and B. M. Weckhuysen, Oxygenated Commodity Chemicals from Chemo-Catalytic Conversion of Biomass Derived Heterocycles, *AIChE J.*, 2018, **64**, 1910–1922.
- 18 S. Yao, X. Wang, Y. Jiang, F. Wu, X. Chen and X. Mu, One-Step Conversion of Biomass-Derived 5-Hydroxymethylfurfural



to 1,2,6-Hexanetriol Over Ni–Co–Al Mixed Oxide Catalysts Under Mild Conditions, *ACS Sustainable Chem. Eng.*, 2013, **2**(2), 173–180.

19 H. Kataoka, D. Kosuge, K. Ogura, J. Ohyama and A. Satsuma, Reductive conversion of 5-hydroxymethylfurfural to 1,2,6-hexanetriol in water solvent using supported Pt catalysts, *Catal. Today*, 2020, **352**, 60–65.

20 T. Tong, Q. Xia, X. Liu and Y. Wang, Direct hydrogenolysis of biomass-derived furans over Pt/CeO<sub>2</sub> catalyst with high activity and stability, *Catal. Commun.*, 2017, **101**, 129–133.

21 T. Mizugaki, T. Yamakawa, Y. Nagatsu, Z. Maeno, T. Mitsudome, K. Jitsukawa and K. Kaneda, Direct Transformation of Furfural to 1,2-pentanediol Using a Hydrotalcite-Supported Platinum Nanoparticle Catalyst, *ACS Sustainable Chem. Eng.*, 2014, **2**, 2243–2247.

22 S. Bhogeswararao and D. Srinivas, Catalytic conversion of furfural to industrial chemicals over supported Pt and Pd catalysts, *J. Catal.*, 2015, **327**, 65–77.

23 T. Uine, J. D. Garber and R. E. Jones, Hydrogenation of 5-hydroxy-Methyl Furfural, US3083236, 1963.

24 J. He, S. P. Burt, M. Ball, D. Zhao, I. Hermans, J. A. Dumesic and G. W. Huber, Synthesis of 1,6-Hexanediol from Cellulose Derived Tetrahydrofuran-Dimethanol with Pt-WO<sub>x</sub>/TiO<sub>2</sub> Catalysts, *ACS Catal.*, 2018, **8**(2), 1427–1439.

25 Y. Shao, J. Wang, K. Sun, G. Gao, M. Fan, C. Li, C. Ming, L. Zhang, S. Zhang and X. Hu, Cu-Based Nanoparticles as Catalysts for Selective Hydrogenation of Biomass-Derived 5-Hydroxymethylfurfural to 1,2-Hexanediol, *ACS Appl. Nano Mater.*, 2022, **5**(4), 5882–5894.

26 M. Sankar, Q. He, M. Morad, J. Pritchard, S. J. Freakley, J. K. Edwards, S. H. Taylor, D. J. Morgan, A. F. Carley, D. W. Knight, C. J. Kiely and G. J. Hutchings, Synthesis of Stable Ligand-free Gold–Palladium Nanoparticles Using a Simple Excess Anion Method, *ACS Nano*, 2012, **6**(8), 6600–6613.

27 M. Sankar, N. Dimitratos, P. J. Miedziak, P. P. Wells, C. J. Kiely and G. J. Hutchings, Designing bimetallic catalysts for a green and sustainable future, *Chem. Soc. Rev.*, 2012, **41**(24), 8099–8139.

28 M. Sankar, Q. He, S. Dawson, E. Nowicka, L. Lu, P. C. A. Bruijnincx, A. M. Beale, C. J. Kiely and B. M. Weckhuysen, Supported bimetallic nano-alloys as highly active catalysts for the one-pot tandem synthesis of imines and secondary amines from nitrobenzene and alcohols, *Catal. Sci. Technol.*, 2016, **6**(14), 5473–5482.

29 Z. Wei, J. Sun, Y. Li, A. K. Datye and Y. Wang, Bimetallic catalysts for hydrogen generation, *Chem. Soc. Rev.*, 2012, **41**(24), 7994–8008.

30 D. M. Alonso, S. G. Wettstein and J. A. Dumesic, Bimetallic catalysts for upgrading of biomass to fuels and chemicals, *Chem. Soc. Rev.*, 2012, **41**(24), 8075–8098.

31 P. Paalanen, B. M. Weckhuysen and M. Sankar, Progress in controlling the size, composition and nanostructure of supported gold–palladium nanoparticles for catalytic applications, *Catal. Sci. Technol.*, 2013, **3**(11), 2869–2880.

32 G. J. Hutchings and C. J. Kiely, Strategies for the Synthesis of Supported Gold Palladium Nanoparticles with Controlled Morphology and Composition, *Acc. Chem. Res.*, 2013, **46**(8), 1759–1772.

33 W. Luo, M. Sankar, A. M. Beale, Q. He, C. J. Kiely, P. C. A. Bruijnincx and B. M. Weckhuysen, High performing and stable supported nano-alloys for the catalytic hydrogenation of levulinic acid to  $\gamma$ -valerolactone, *Nat. Commun.*, 2015, **6**(1), 6540.

34 S. Guadix-Montero, A. Santos Hernandez, N. Lei, D. J. Morgan, Q. He, A. Wang, T. Zhang, A. Roldan and M. Sankar, Controlling the Selectivity of Supported Ru Nanoparticles During Glycerol Hydrogenolysis: C–O vs C–C Cleavage, *ChemCatChem*, 2021, **13**(6), 1595–1606.

35 C. E. Mitchell, U. Terranova, I. Alshibane, D. J. Morgan, T. E. Davies, Q. He, J. S. Hargreaves, M. Sankar and N. H. de Leeuw, Liquid phase hydrogenation of CO<sub>2</sub> to formate using palladium and ruthenium nanoparticles supported on molybdenum carbide, *New J. Chem.*, 2019, **43**(35), 13985–13997.

36 A. Fihri, C. Len, R. S. Varma and A. Solhy, Hydroxyapatite: A review of syntheses, structure and applications in heterogeneous catalysis, *Coord. Chem. Rev.*, 2017, **347**, 48–76.

37 H. Brasil, A. F. B. Bittencourt, K. C. E. S. Yokoo, P. C. D. Mendes, L. G. Verga, K. F. Andriani, R. Landers, J. L. F. Da Silva and G. P. Valenca, Synthesis modification of hydroxyapatite surface for ethanol conversion: The role of the acidic/basic sites ratio, *J. Catal.*, 2021, **404**, 802–813.

38 T. Tsuchida, J. Kubo, T. Yoshioka, S. Sakuma, T. Takeguchi and W. Ueda, Reaction of ethanol over hydroxyapatite affected by Ca/P ratio of catalyst, *J. Catal.*, 2008, **259**(2), 183–189.

39 S. J. Joris and C. H. Amberg, The Nature of Deficiency in Nonstoichiometric Hydroxyapatites. I. Catalytic Activity of Calcium and Strontium Hydroxyapatites, *J. Phys. Chem.*, 1971, **75**, 3167.

40 S. Diallo-Garcia, M. B. Osman, J.-M. Krafft, S. Casale, C. Thomas, J. Kubo and G. Costentin, Identification of Surface Basic Sites and Acid–Base Pairs of Hydroxyapatite, *J. Phys. Chem. C*, 2014, **118**(24), 12744–12757.

41 L. Silvester, J.-F. Lamonier, J. Faye, M. Capron, R.-N. Vannier, C. Lamonier, J. Dubois, J. Couturier, C. Calais and F. Dumeignil, Reactivity of ethanol over hydroxyapatite-based Ca-enriched catalysts with various carbonate contents, *Catal. Sci. Technol.*, 2015, **5**(5), 2994–3006.

42 M. B. Osman, S. D. Garcia, J.-M. Krafft, C. Methivier, J. Blanchard, T. Yoshioka, J. Kubo and G. Costentin, Control of calcium accessibility over hydroxyapatite by post-precipitation steps: influence on the catalytic reactivity toward alcohols, *Phys. Chem. Chem. Phys.*, 2016, **18**(40), 27837–27847.

43 H. Alsharif, M. B. Conway, D. J. Morgan, T. E. Davies, S. H. Taylor and M. Sankar, Controlling the nanoparticle size and shape of a Pt/TiO<sub>2</sub> catalyst for enhanced hydrogenation of furfural to furfuryl alcohol, *RSC Sustainability*, 2024, **2**(12), 3888–3896.

44 N. Fairley, V. Fernandez, M. Richard-Plouet, C. Guillot-Deudon, J. Walton, E. Smith, D. Flahaut, M. Greiner, M.



Biesinger, S. Tougaard, D. Morgan and J. Baltrusaitis, Systematic and collaborative approach to problem solving using X-ray photoelectron spectroscopy, *Appl. Surf. Sci. Adv.*, 2021, **5**, 100112.

45 S. Wang, V. Vorotnikov and D. G. Vlachos, A DFT study of furan hydrogenation and ring opening on Pd(111), *Green Chem.*, 2014, **16**(2), 736–747.

46 Z. Xu, G. Huang, Z. Yan, N. Wang, L. Yue and Q. Liu, Hydroxyapatite-Supported Low-Content Pt Catalysts for Efficient Removal of Formaldehyde at Room Temperature, *ACS Omega*, 2019, **4**(26), 21998–22007.

47 NIST X-ray Photoelectron Spectroscopy Database, NIST Standard Reference Database Number 20, National Institute of Standards and Technology, Gaithersburg MD, 2000, p. 20899, DOI: [10.18434/T4T88K](https://doi.org/10.18434/T4T88K), (retrieved [date of access]).

48 D. J. Morgan, Resolving ruthenium: XPS studies of common ruthenium materials, *Surf. Interface Anal.*, 2015, **47**(11), 1072–1079.

